Title	InGaP grown on Ge (100) by molecular beam epitaxy: a spectroscopic ellipsometry study
Author(s)	D'Costa, Vijay Richard; Loke, Wan Khai; Zhou, Qian; Yoon, Soon Fatt; Yeo, Yee-Chia
Citation	D'Costa, V. R., Loke, W. K., Zhou, Q., Yoon, S. F., & Yeo, Y.-C. (2016). InGaP grown on Ge (100) by molecular beam epitaxy: a spectroscopic ellipsometry study. Semiconductor Science and Technology, 31(3), 035022-.
Date	2016
URL	http://hdl.handle.net/10220/40554
Rights	© 2016 IOP Publishing Ltd. This is the author created version of a work that has been peer reviewed and accepted for publication by Semiconductor Science and Technology, IOP Publishing Ltd. It incorporates referee's comments but changes resulting from the publishing process, such as copyediting, structural formatting, may not be reflected in this document. The published version is available at: [http://dx.doi.org/10.1088/0268-1242/31/3/035022].

InGaP grown on Ge (100) by molecular beam epitaxy: A spectroscopic ellipsometry study

Vijay Richard D'Costa[1,a)], Wan Khai Loke[2], Qian Zhou[1], Soon Fatt Yoon[2], and Yee-Chia Yeo[1,b)]

[1]*Department of Electrical and Computer Engineering, National University of Singapore, Singapore 117583*

[2]*School of Electrical and Electronic Engineering, Nanyang Technological University, Singapore 639798*

[a)] Electronic mail: elevrd@nus.edu.sg

[b)] Electronic mail: eleyeoyc@nus.edu.sg

ABSTRACT

We investigated the optical properties of disordered $In_{0.52}Ga_{0.48}P$ alloys by spectroscopic ellipsometry in the far-infrared to ultraviolet energy range (0.037 – 5.1 eV). The alloys were grown on Ge (100) substrate by solid-source molecular beam epitaxy. The far-infrared dielectric function reveals two absorption peaks that can be attributed to InP- and GaP-like vibrational modes. The visible-UV dielectric function of $In_{0.52}Ga_{0.48}P$ alloys nearly lattice-matched to Ge shows the critical points E_0, E_1, and E_2, energies of which are determined using a derivative analysis. A weak transition that can be identified as the $E_1 + \Delta_1$ critical point is revealed. The vibrational frequencies and the transition energies in $In_{0.52}Ga_{0.48}P$ are lower relative to $In_{0.49}Ga_{0.51}P$ lattice-matched to GaAs. The downward shifts in E_0 and phonons can be estimated using the compositional dependence of E_0 and phonons of bulk alloys.

Integration of III-V semiconductors with group-IV substrates has attracted considerable interest for its potential in various electronic and optical devices. $In_xGa_{1-x}P$ alloy, which is lattice-matched to GaAs at $x = 0.49$ and can lattice-match Ge at 0.50, has applications in multi-junction solar cells.[1] InGaP is reported to form a type-I band alignment with Ge, offering large valence and conduction band offsets (~ 0.6 eV) with respect to Ge.[2] As reported for Ge *p*-metal-oxide-semiconductor-field-effect-transistors (MOSFETs) and *n*-MOSFETS capped with a thin lattice-matched InAlP layer,[3] InGaP instead of InAlP could also lead to confinement of electrons and holes within the Ge channel. InAlP/Ge heterostructure provides an average band offset of ~0.85 eV for both valence and conduction bands.[4] The separation of carriers from the dielectric/InAlP interface minimizes scattering from interface traps leading to high carrier mobilities. This makes InGaP a viable candidate as a surface passivation layer for Ge in future MOSFETs. From a fundamental physics perspective, $In_{0.49}Ga_{0.51}P$ is an interesting system as it shows structural ordering (CuPt-type) depending on the growth conditions.[5-8] For a given alloy composition, this ordering can cause shifts in the electronic transitions and may introduce additional electronic transitions and vibrational modes relative to disordered alloys.[9-13]

The electronic and vibrational properties of ordered and disordered InGaP alloys can be evaluated using the complex dielectric function obtained from spectroscopic ellipsometry. Spectroscopic ellipsometry studies of ordered as well as disordered InGaP alloys grown on GaAs by various growth techniques are discussed in literature.[10,12,14,15] A few studies on growth and characterization of InGaP on Ge substrate were reported.[16-21] Photoluminescence characterization has shed some light on the bandgap of ordered and disordered InGaP on Ge.[16,18] However, a detailed investigation of electronic bandstructure of InGaP grown on Ge is currently lacking in literature.

In this paper, we use spectroscopic ellipsometry to investigate the electronic bandstructure of $In_{0.52}Ga_{0.48}P$ alloys grown on Ge by solid-source molecular beam epitaxy (MBE). The far-infrared to ultraviolet dielectric function shows the critical points E_0, E_1, and E_2 in the visible-UV range and the vibrational modes in the far-infrared range. The energy transitions and the vibrational frequencies of $In_{0.52}Ga_{0.48}P$ on Ge are consistent with InGaP lattice-matched to GaAs if we take into account the difference in composition between the two alloys.

A ~ 560 nm thick InGaP film was grown on a Ge (100) substrate having a 6^o offcut towards <111> using a solid-source MBE equipped with indium (In), gallium (Ga), and phosphorus (P) valved cracker sources. The Ge wafer was first cleaned using a diluted hydrofluoric acid and immediately loaded into the MBE system. Prior to epitaxial growth, the Ge wafer was heated to 650 ^{0}C for 30 minutes for double atomic step formation. Then, the Ge wafer was cooled to 330 ^{0}C for the growth of the InGaP film. In and Ga fluxes used were 5.81×10^{13} atoms/cm^2/s and 5.88×10^{13} atoms/cm^2/s, respectively. The growth rate for InGaP was 0.53 Å/s.

The structural quality of the sample was evaluated using cross-sectional transmission electron microscopy (TEM) and high-resolution X-ray diffractometry (HR-XRD). Cross-sectional TEM images in Figs. 1(a) and 1(b) indicate that the InGaP film is of uniform thickness with a clear interface between the film and the substrate. Transmission-electron-diffraction (TED) pattern shown in Figure 1(c) was also acquired to verify whether CuPt-type ordering is present in the InGaP film. Superlattice spots that could be associated with atomic ordering were not observed. Fig. 2 shows the (224) reciprocal space mapping (RSM) obtained by HR-XRD. The in-plane reciprocal lattice vector q_x of the InGaP alloy is nearly aligned with that of Ge substrate indicating that InGaP is nearly lattice-matched to Ge. The in-plane strain $\varepsilon_{\|}$ and the In

composition x calculated from the RSM are ~ -0.15% and 0.52, respectively. InGaP that is perfectly lattice-matched to Ge could be attained by fine-tuning In and Ga fluxes in addition to taking into account the small thermal expansion coefficient mismatch between InGaP and Ge.

Woollam's variable angle spectroscopic ellipsometer (VASE) and an infrared variable angle spectroscopic ellipsometer (IR-VASE) were used for acquisition of ellipsometric angles Ψ and Δ. The data was acquired at two angles of incidence, 50° and 70°, from 0.7 to 5.1 eV on the VASE. IR-VASE was used to acquire the data from 298 to 6049 cm^{-1} (0.037 to 0.75 eV) at 65° with a resolution of 2 cm^{-1}. The experimental pseudo-dielectric function from near-infrared to ultraviolet, $<\varepsilon>_{NIR-UV}$, obtained from Ψ and Δ acquired at an angle of incidence of 70° is shown in Fig. 3(a). Although the pseudo-dielectric function represents the optical response of the entire sample (surface layer − film − substrate), it often provides useful insights into the dielectric response of the film. The critical points E_1 and E_2 are clearly observed whereas E_0 is masked by the presence of interference oscillations. The experimental far-infrared pseudo-dielectric function $<\varepsilon>_{FIR}$ obtained from Ψ and Δ acquired at an angle of incidence of 65° is shown in Fig. 4(a). Strong absorption in the far-infrared is seen which can be attributed to the vibrational modes in InGaP.

To obtain the dielectric function of the InGaP layer, the sample was modeled as a three-layer structure consisting of a bottom-most Ge substrate, InGaP film, and a surface layer. The surface film was modeled as an effective medium consisting of 50% voids and 50% InGaP.[22] The dielectric function of Ge substrate was taken from literature.[23] The complex dielectric function of InGaP layer in 0.7 – 5.1 eV energy range is modeled using three Kramers-Kronig consistent oscillators[24] that describe the critical point transitions E_0, E_1, and E_2. The far-infrared

to mid-infrared response was described using two Lorentzian oscillators that account for absorption due to InP- and GaP-like vibrational modes.

The InGaP parametric optical constants, the InGaP film thickness, and the surface film thickness were obtained simultaneously using standard ellipsometric data fitting procedures.[25] The point-by-point dielectric function of the InGaP layer was then extracted on a wavelength-by-wavelength basis using fixed thicknesses determined in the previous step.[26] Near-infrared to ultraviolet and far-infrared point-by-point dielectric functions obtained for the $In_{0.52}Ga_{0.48}P$ alloys are shown in Figs. 3(b) and 4(b), respectively. The agreement between the model and point-by-point dielectric functions is excellent, guaranteeing Kramers-Kronig consistency of the point-by-point function.

The near-infrared to ultraviolet point-by-point dielectric function contains a few numerical artifacts (indicated by arrows) near the E_0 gap. These artifacts may arise due to deviation in the optical constants of the substrate and surface layer from their true values.[25] The deviation of fixed thicknesses of the films assumed in the point-by-point analysis from their true thickness values may also lead to artifacts in the dielectric function.[25] Although the point-by-point fit is successful indicating that the three-layer structure represents the sample adequately, the presence of artifacts in the dielectric function of the film might indicate that there is still some room for accurate description of the sample. We considered the possibility that an interfacial layer may exist between InGaP and Ge. The interface layer was modeled as an effective medium consisting of 50% InGaP and 50% Ge. However, inclusion of this additional layer in the sample structure does not improve the fit to the data as evaluated by mean-squared-error compared with the sample model without it. Although the physical presence of the interface

layer cannot be ruled out, adding complexity to sample model does not improve sensitivity to the data including the removal of artifacts in the point-by-point dielectric function.

The far-infrared dielectric function reveals two peaks – one stronger in intensity than the other – with their relative strength being consistent with previous reports on disordered InGaP alloys lattice-matched to GaAs.[9,14] The stronger peak observed at 329.3 cm^{-1} and the weaker peak at 369.9 cm^{-1} can be associated with InP- and GaP-like vibrations, respectively.[9] The downward shift in phonon frequencies of ~ 2 – 3 cm^{-1} may be attributed to the presence of higher In content in the alloy relative to the InGaP alloy lattice-matched to GaAs. In fact, our estimates of ~ 329.6 cm^{-1} and ~ 368.6 cm^{-1} for the two modes using the compositional dependence of phonons in InGaP are in very good agreement with observed values.[27,28] The direct bandgap E_0 of InGaP on Ge is now clearly observed in the visible-ultraviolet dielectric function. The near-infrared to ultraviolet dielectric function of $In_{0.49}Ga_{0.51}P$ lattice-matched to GaAs (Ref. [15]) is shown for comparison in Fig. 3(b). The overall agreement between the dielectric functions of $In_{0.52}Ga_{0.48}P$ on Ge and $In_{0.49}Ga_{0.51}P$ on GaAs is quite good. Consistent with the downward shift observed for phonons, the dielectric function of $In_{0.52}Ga_{0.48}P$ is shifted to the left relative to $In_{0.49}Ga_{0.51}P$.

We used numerical second-order derivatives to obtain the parameters associated with E_0, E_1, and E_2 critical points. The point-by-point dielectric function with an energy step size of 0.01 eV was differentiated using 17 Savitzky-Golay smoothing coefficients for second-order derivatives with a polynomial of order 5. The derivatives of the point-by-point dielectric function were fitted using an analytic expression[26]

$$\frac{d^2\varepsilon_{visible-UV}}{dE^2} = \frac{A_{E_0}e^{i\Phi_{E_0}}}{[E - E_0 + i\Gamma_{E_0}]^{3/2}} + \sum_j \frac{A_j e^{i\Phi_j}}{[E - E_j + i\Gamma_j]^2}, \quad (1)$$

where A_{E_0}, Φ_{E_0}, E_0, and Γ_{E_0} are the amplitude, phase angle, energy transition, and broadening parameters associated with the E_0 critical point. The second term describes E_1, $E_1+\Delta_1$, and E_2 critical points. A_j, Φ_j, E_j, and Γ_j are the critical point parameters associated with each critical point. Although the fits to Ψ and Δ do not require an oscillator corresponding to $E_1+\Delta_1$ critical point, the fit to numerical second-order derivatives of the dielectric function improves noticeably with the inclusion of $E_1+\Delta_1$.

Fig. 5 shows numerical second-order derivatives for the E_0 critical point along with the model fit using Eq. (1). Besides the E_0 feature, which is described well by Eq. (1), additional oscillatory features are observed. We identify the E_0 feature unambiguously by using the second derivative of the parametric dielectric function as a guide. The origin of the sharp oscillatory features in the second derivatives in the energy range between 2 and 2.5eV could be traced to the numerical artifacts in the point-by-point dielectric function (Fig. 3(b)). Although the derivative analysis enhances critical point features, it also tends to worsen the signal-to-noise ratio of the experimental data in the region around the bandgap even in the absence of visible artifacts. The second-order derivatives for E_1 and E_2 critical points in the UV energy range are shown in Fig. 6. The fits with and without the inclusion of weak $E_1+\Delta_1$ are also shown and the improvement in the fit with $E_1+\Delta_1$ is clear. In the absence of ordering in the sample, we assigned this weak feature as $E_1+\Delta_1$ as it is consistent with the magnitude of spin-orbit splitting.[29] Alsina *et al.*[30] observed splitting in E_1 transition in ordered alloys. However, the splitting associated with ordering is ~ 0.04 – 0.06 eV in partially ordered InGaP which is much smaller than Δ_1 = 0.185 eV. Our findings and the assignment of this weak critical point as $E_1+\Delta_1$ is consistent with the previous work by Lee *et al.*[27,31] on disordered InGaP lattice-matched to GaAs. Even in their ordered alloys, despite including an additional feature associated with ordering, numerical

derivative analysis was still sensitive to $E_1+\Delta_1$.[12] On the other hand, Schubert *et al.*[15] did not observe the weak $E_1+\Delta_1$ critical point in disordered InGaP alloys lattice-matched to GaAs.

A fit using Eq. (1) gives all the critical point parameters associated with E_0, E_1, $E_1+\Delta_1$, and E_2 transitions of $In_{0.52}Ga_{0.48}P$ alloys. The energy parameters are summarized in Table I, along with reference values from literature. It must be pointed out that the amplitudes, broadenings, and phase angles, including those for the weak $E_1+\Delta_1$ feature, are in excellent agreement with those obtained by Lee *et al.*[12,31] All the transitions are shifted down with respect to the $In_{0.49}Ga_{0.51}P$ alloy lattice-matched to GaAs. Alloy effect, which is the difference in In and Ga compositions between $In_{0.52}Ga_{0.48}P$ on Ge and $In_{0.49}Ga_{0.51}P$ on GaAs, and epitaxial strain should contribute to the energy shifts with respect to the reference sample. We assume that the contribution from ordering to the energy shifts is negligible as the TED pattern did not reveal any superlattice spots.

We can analyze E_0, E_1 and $E_1+\Delta_1$ transitions in InGaP using the deformation potential theory[32] and the known compositional dependence of the relaxed alloys.[29,33] The deformation potential theory allows estimation of energy shifts due to strain. Shear deformation potentials, which are required to estimate the effect of strain on E_1 and $E_1+\Delta_1$ individually, are not available for the one of the endpoint materials, GaP. Shear deformation potential for InGaP is obtained by a linear interpolation of shear deformation potentials for InP and GaP. Since the strain-induced energy shift for the average of E_1 and $E_1+\Delta_1$, $\bar{E}_1$ is given by $\Delta\bar{E}_1 = (2/\sqrt{3})D_1^1\left(1-c_{12}/c_{11}\right)\varepsilon_{\square}$, we need only the hydrostatic deformation potentials which are available for both InP and GaP. D_1^1 is the hydrostatic deformation potential obtained by a linear interpolation of the values for binary materials. $c_{11} = 12.1 \times 10^{11}$ dynes/cm^2 and $c_{12} = 6.0 \times 10^{11}$ dynes/cm^2 are the elastic constants for

InGaP obtained by a linear interpolation of the values for InP and GaP.[34] $\bar{E}_1$ shows an average downward shift of ~ 29 meV whereas E_0 shows an average downward shift of ~ 47 ± 25 meV relative to $In_{0.49}Ga_{0.51}P$ on GaAs. The total energy shift for $\bar{E}_1$ lies within its experimental error and hence, we do not analyze it further. The compressive strain in the epitaxial film is expected to raise E_0. The strain-induced energy shift for E_0 can be estimated using $\Delta E_0 = \varepsilon_{\square}\left[2a\left(1-\frac{c_{12}}{c_{11}}\right)-b\left(1+2\frac{c_{12}}{c_{11}}\right)\right]$, where a = -8.0 and b = -1.75 are the deformation potentials for the InGaP alloy obtained by a linear interpolation of values for InP and GaP.[34] We obtained ΔE_0 of ~ 6 meV. The energy shift for E_0 due to the alloy effect can be estimated using the compositional dependence of relaxed InGaP alloys.[29,33] It could cause a downward shift of up to ~ 43 meV in $In_{0.52}Ga_{0.48}P$ relative to $In_{0.49}Ga_{0.51}P$. The estimated energy shift for E_0 due to combined effect of strain and alloy effect is ~ 37 meV with the alloy effect clearly dominating the energy shift. This is in reasonable agreement with the total energy shift considering the scatter of E_0 values from literature.

The broadening parameters, which are a measure of film quality, are comparable to those for InGaP lattice-matched to GaAs for E_1 and E_2.[12,31] Although a few dislocations are visible in cross-sectional TEM (image is not shown here) along the interface, the agreement of broadening parameters with those for InGaP lattice-matched to GaAs can be attributed to the fact that the light around these transitions mainly probes the top region of the film. The bulk of the film did not show any dislocations in cross-sectional TEM. The broadening parameters associated with E_0 may be influenced by the presence of the dislocations since the light probes the entire film in this energy range. Unfortunately, broadening parameters for E_0 using analysis similar to ours are not reported for InGaP lattice-matched to GaAs to allow a direct comparison. We believe that we can

further improve the quality of the film by optimizing growth conditions, including fine-tuning of In or Ga composition to lattice-match InGaP to Ge.

In conclusion, we studied the optical properties of InGaP alloys grown on Ge (100) using spectroscopic ellipsometry in the far-infrared to ultraviolet range. The complex dielectric function of the InGaP alloy revealed the critical points E_0, E_1, $E_1+\Delta_1$, and E_2 in addition to InP- and GaP-like vibrational modes in the far-infrared. The energy transitions were obtained using a critical point analysis. The experimental E_0 and phonon shifts in $In_{0.52}Ga_{0.48}P$ relative to $In_{0.49}Ga_{0.51}P$ alloy lattice-matched to GaAs can be explained using the compositional dependence of bulk InGaP alloys.

This work was supported by the National Research Foundation under the Competitive Research Programme (Grant No. NRF-CRP6-2010-4). We are grateful to Dr. Mathias Schubert for providing us with the optical constants of disordered InGaP lattice-matched to GaAs.

[1] R. R. King, D. C. Law, K. M. Edmondson, C. M. Fetzer, G. S. Kinsey, H. Yoon, R. A. Sherif, and N. H. Karam, Applied Physics Letters **90** (18), 183516 (2007).

[2] M. H. S. Owen, Q. Zhou, X. Gong, Z. Zhang, J. S. Pan, W. K. Loke, S. Wicaksono, S. F. Yoon, E. S. Tok, and Y.-C. Yeo, Applied Physics Letters **105** (10), 101604 (2014).

[3] B. Liu, X. Gong, R. Cheng, P. Guo, Q. Zhou, M. H. S. Owen, C. Guo, L. Wang, W. Wang, Y. Yang, Y.-C. Yeo, C.-T. Wan, S.-H. Chen, C.-C. Cheng, Y.-R Lin, C.-H. Wu, C.-H. Ko, and C. H. Wann, in *Electron Devices Meeting (IEDM), 2013 IEEE International* (2013), pp. 26.7.1.

[4] M. H. S. Owen, C. Guo, S.-H. Chen, C.-T. Wan, C.-C. Cheng, C.-H. Wu, C.-H. Ko, C. H. Wann, Ivana, Z. Zhang, J. S. Pan, and Y.-C. Yeo, Applied Physics Letters **103** (3), 031604 (2013).

[5] A. Gomyo, T. Suzuki, and S. Iijima, Physical Review Letters **60** (25), 2645 (1988).

[6] S. R. Kurtz, J. M. Olson, and A. Kibbler, Applied Physics Letters **57** (18), 1922 (1990).

[7] K. Sinha, A. Mascarenhas, R. G. Alonso, G. S. Horner, K. A. Bertness, S. R. Kurtz, and J. M. Olson, Solid State Communications **89** (10), 843 (1994).

[8] L. C. Su, I. H. Ho, and G. B. Stringfellow, Journal of Applied Physics **75** (10), 5135 (1994).

[9] F. Alsina, J. D. Webb, A. Mascarenhas, J. F. Geisz, J. M. Olson, and A. Duda, Physical Review B **60** (3), 1484 (1999).

[10] T. Hofmann, V. Gottschalch, and M. Schubert, Physical Review B **66** (19), 195204 (2002).
[11] F. Alsina, N. Mestres, J. Pascual, C. Geng, P. Ernst, and F. Scholz, Physical Review B **53** (19), 12994 (1996).
[12] H. Lee, M. V. Klein, J. M. Olson, and K. C. Hsieh, Physical Review B **53** (7), 4015 (1996).
[13] S.-H. Wei and A. Zunger, Physical Review B **57** (15), 8983 (1998).
[14] T. Hofmann, G. Leibiger, V. Gottschalch, I. Pietzonka, and M. Schubert, Physical Review B **64** (15), 155206 (2001).
[15] M. Schubert, J. A. Woollam, G. Leibiger, B. Rheinländer, I. Pietzonka, T. Sab, and V. Gottschalch, Journal of Applied Physics **86** (4), 2025 (1999).
[16] W. He, S. L. Lu, J. R. Dong, Y. M. Zhao, X. Y. Ren, K. L. Xiong, B. Li, H. Yang, H. M. Zhu, and X. Y. Chen, Applied Physics Letters **97** (12), 121909 (2010).
[17] P. J. Sophia, G. Attolini, M. Bosi, E. Buffagni, C. Ferrari, C. Frigeri, K. Vad, A. Csik, V. Takáts, and Z. Zolnai, ECS Journal of Solid State Science and Technology **4** (3), P53 (2015).
[18] H.-M. Wu, S.-J. Tsai, Y.-Chi Chang, Y.-R. Chen, and H.-H. Lin, Thin Solid Films **570**, 390 (2014).
[19] C. Yang, K. Shin, J. Kim, J. Lee, E. Yoon, C. -Z. Kim, H. Kang, and W. Park, (2010).
[20] J. W. Baek, J. Shim, and J.-H. Park, Current Applied Physics **15** (7), 765 (2015).
[21] W. K. Loke, Q. Zhou, X. Gong, M. H. S. Owen, S. Wicaksono, K. H. Tan, Y.-C. Yeo, and S. F. Yoon, in *Silicon-Germanium Technology and Device Meeting (ISTDM), 2014 7th International* (IEEE, 2014), pp. 75.
[22] C. F. Bohren and D. R. Huffman, *Absorption and Scattering of Light by Small Particles*. (Wiley Interscience, New York, 1983), p.530.
[23] R. F. Potter, in *Handbook of Optical Constants of Solids*, edited by Edward D. Palik (Academic Press, Burlington, 1997), pp. 465.
[24] B. Johs, C. M. Herzinger, J. H. Dinan, A. Cornfeld, and J. D. Benson, Thin Solid Films **313–314** (0), 137 (1998).
[25] H. Tompkins and E. A. Irene, *Handbook of ellipsometry*. (William Andrew, 2005).
[26] V. R. D'Costa, C. S. Cook, A. G. Birdwell, C. L. Littler, M. Canonico, S. Zollner, J. Kouvetakis, and J. Menendez, Physical Review B **73** (12), 125207 (2006).
[27] H. Lee, D. Biswas, M. V. Klein, H. Morkoc, D. E. Aspnes, B. D. Choe, J. Kim, and C. O. Griffiths, Journal of Applied Physics **75** (10), 5040 (1994).
[28] E. Bedel, R. Carles, G. Landa, and J. B. Renucci, Revue de Physique Appliquée **19** (1), 17 (1984).
[29] C. Alibert, G. Bordure, A. Laugier, and J. Chevallier, Physical Review B **6** (4), 1301 (1972).
[30] F. Alsina, M. Garriga, M. I. Alonso, J. Pascual, J. Camassel, and R. W. Glew, Materials Science and Technology **14** (12), 1283 (1998).
[31] H. Lee, M. V. Klein, D. E. Aspnes, C. P. Kuo, M. Peanasky, and M. G. Craford, Journal of Applied Physics **73** (1), 400 (1993).
[32] F. H. Pollak, in *Semiconductors and Semimetals*, edited by P. P. Thomas (Elsevier, 1990), Vol. Volume 32, pp. 17.
[33] H. Lange, J. Donecker, and H. Friedrich, Physica Status Solidi (b) **73** (2), 633 (1976).

[34] O. Madelung, in *Landolt-Börnstein, Numerical Data and Functional Relationships in Science and Technology* (Springer-Verlag, Berlin, 1982), Vol. 17a.
[35] M. Schubert, V. Gottschalch, C. M. Herzinger, H. Yao, P. G. Snyder, and J. A. Woollam, Journal of Applied Physics **77** (7), 3416 (1995).

TABLES

Table I

Energy transitions for InGaP alloy grown on Ge.

Parameter	$In_{0.52}Ga_{0.48}P$ on Ge	$In_{0.49}Ga_{0.51}P$
	This work	Other work
E_0 (eV)	1.826 ± 0.004	1.87[a], 1.86[a], 1.85[a] 1.899[b], 1.887[c]
E_1 (eV)	3.210 ± 0.010	3.224[b], 3.256[d], 3.245[e]
$E_1 + \Delta_1$ (eV)	3.418 ± 0.031	3.441[d], 3.430[e]
Δ_1 (eV)	0.208 ± 0.031	0.185[d], 0.185[e]
E_2 (eV)	4.815 ± 0.012	4.832[b], 4.864[d]

[a] Ref. [35]
[b] Ref. [15]
[c] Ref. [33]
[d] Ref. [29]
[e] Ref. [31]

Figure Captions

FIG. 1. (a) Low magnification cross-sectional TEM image showing the epitaxial ~ 560 nm thick $In_{0.52}Ga_{0.48}P$ film on Ge substrate. (b) High magnification cross-sectional TEM image indicating clear interface between InGaP and Ge. (c) [011] zone-axis TED pattern for the InGaP layer revealing the absence of CuPt-type atomic ordering in the film.

FIG. 2. HR-XRD (224) RSM for the InGaP alloy grown on Ge (100). The in-plane reciprocal lattice vector q_x for InGaP and Ge are nearly identical indicating that the InGaP film is nearly lattice-matched to Ge.

FIG. 3. (a) Experimental (dotted) and model (solid) visible-UV pseudo-dielectric functions for the ~ 560 nm thick InGaP-on-Ge sample. The experimental pseudo-dielectric function was obtained from Ψ and Δ acquired at an angle of incidence of 70°. (b) Point-by-point (solid black line) and model (solid gray line) visible-UV dielectric functions of the InGaP film. The dielectric function of a disordered $In_{0.49}Ga_{0.51}P$ from Ref. [15] (dotted) is also shown for reference.

FIG. 4. (a) Experimental (dotted) and model (solid) far-infrared pseudo-dielectric functions for the ~ 560 nm thick InGaP-on-Ge sample. The experimental pseudo-dielectric function was obtained from Ψ and Δ acquired at an angle of incidence of 65°. (b) Point-by-point (dotted) and model (solid) far-infrared dielectric functions of the InGaP film. The features at 329.3 cm^{-1} and 369.9 cm^{-1} in the dielectric response correspond to InP-like and GaP-like vibrations, respectively.

FIG. 5. Numerical second derivatives of (a) real and (b) imaginary parts of the visible dielectric function for InGaP showing the E_0 critical point. Point-by-point data is plotted in circles and the model fit using Eq. (1) is plotted using solid gray line. Numerical second derivatives of the parametric dielectric function (solid black line) were used as a guide to identify E_0 correctly in the presence of numerical artifacts in this energy range.

FIG. 6. Numerical second derivatives of (a) real and (b) imaginary parts of the dielectric function for InGaP showing E_1 and E_2 critical points. Point-by-point data is plotted in circles and the model fit using Eq. (1) is plotted using solid gray line. Model fit without the inclusion of $E_1 + \Delta_1$ (black solid line) is also shown for comparison.

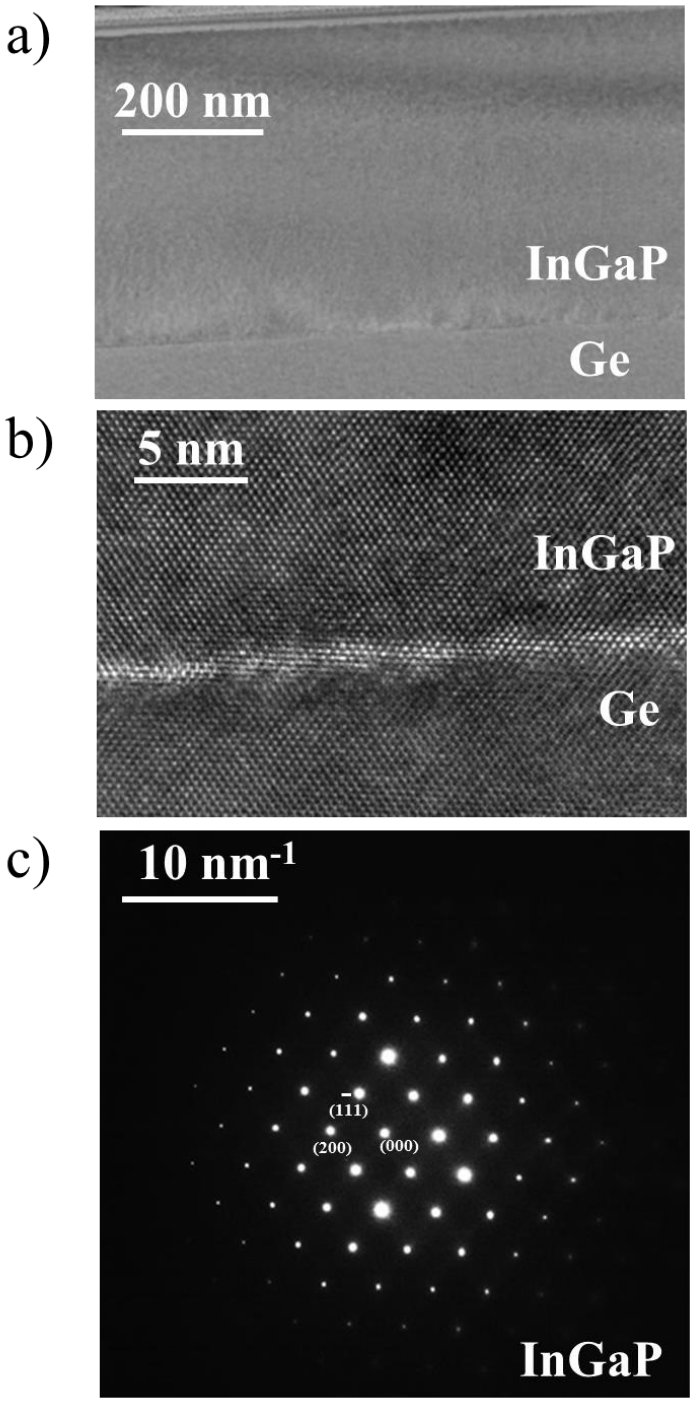

FIG. 1

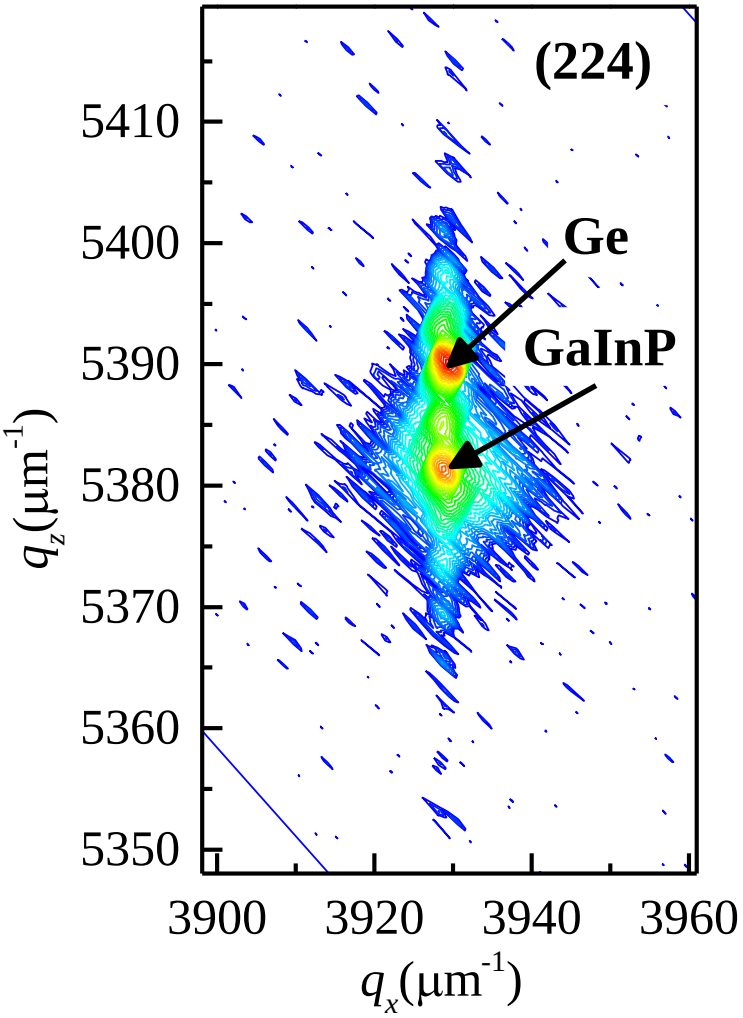
(224)
Ge
GaInP
5410
5400
5390
5380
5370
5360
5350
3900
3920
3940
3960
$q_z(\mu m^{-1})$
$q_x(\mu m^{-1})$

FIG. 2

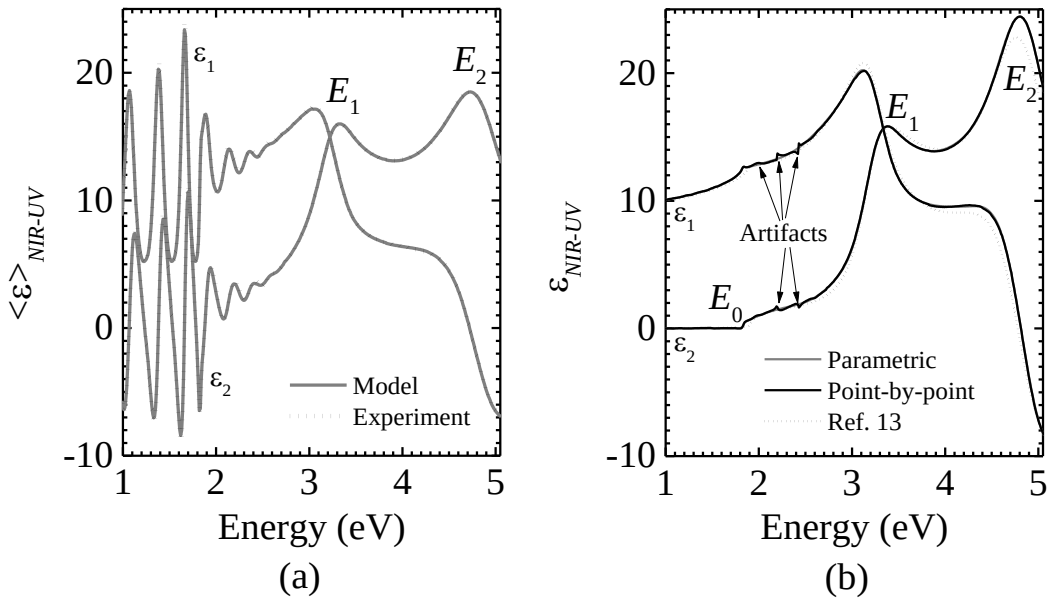
20
10
0
-10
1
2
3
4
5
Energy (eV)
(a)
$\langle\varepsilon\rangle_{NIR\text{-}UV}$
ε_1
ε_2
E_1
E_2
Model
Experiment
$\varepsilon_{NIR\text{-}UV}$
Artifacts
E_0
Parametric
Point-by-point
Ref. 13
(b)

FIG. 3

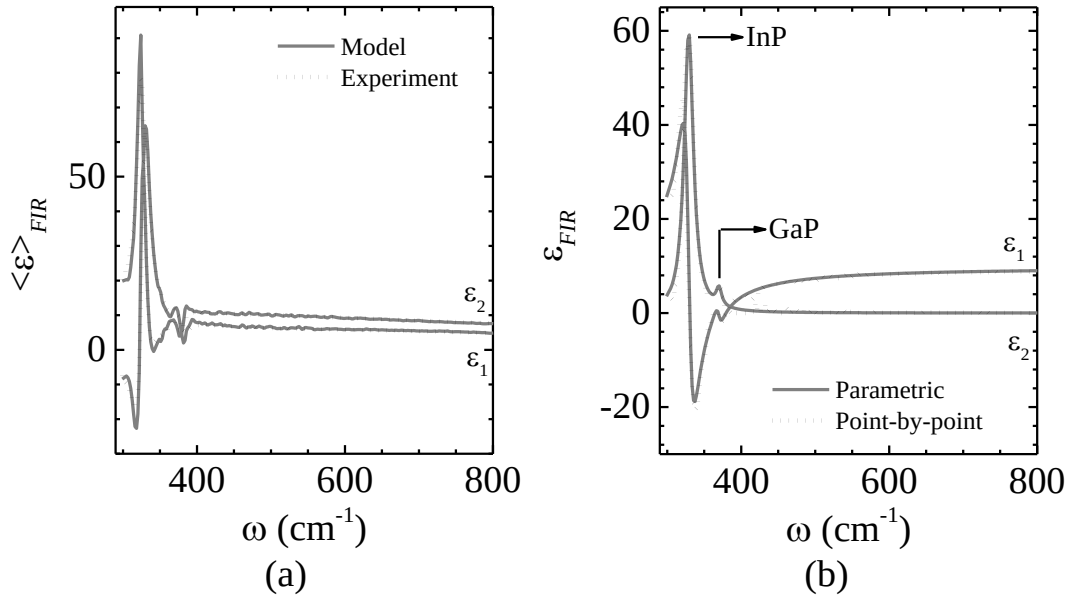
Model
Experiment
50
0
ε_2
ε_1
400
600
800
ω (cm^{-1})
(a)
60
40
20
0
-20
InP
GaP
ε_1
ε_2
Parametric
Point-by-point
400
600
800
ω (cm^{-1})
(b)

FIG. 4

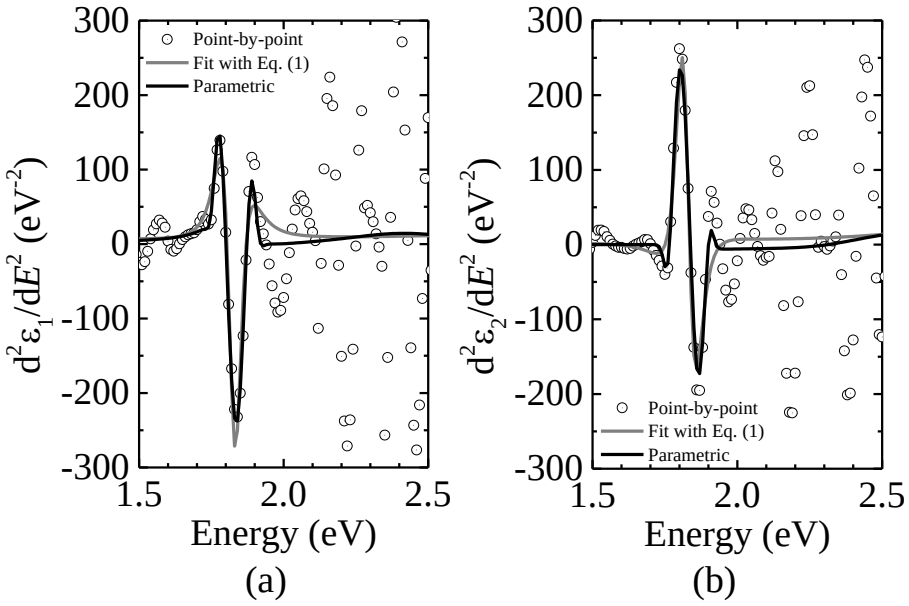
Point-by-point
Fit with Eq. (1)
Parametric
$d^2\varepsilon_1/dE^2$ (eV^{-2})
Energy (eV)
(a)
$d^2\varepsilon_2/dE^2$ (eV^{-2})
Energy (eV)
(b)

FIG. 5

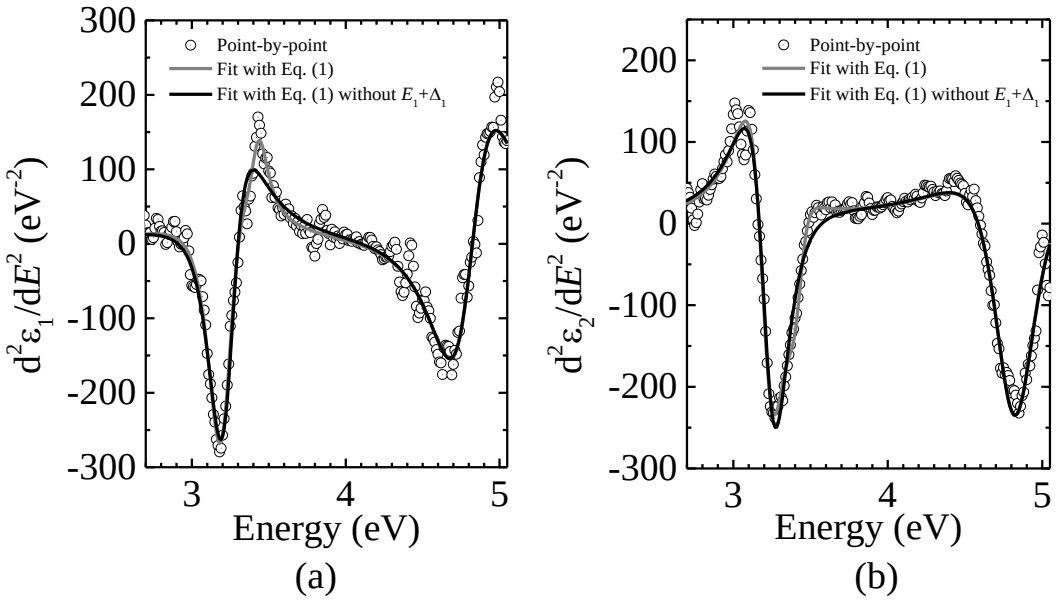
Point-by-point
Fit with Eq. (1)
Fit with Eq. (1) without $E_1+\Delta_1$
$d^2\varepsilon_1/dE^2$ (eV^{-2})
$d^2\varepsilon_2/dE^2$ (eV^{-2})
Energy (eV)
(a)
(b)

FIG. 6